**Proceedings of the ASME 2023**
**International Mechanical Engineering Congress and Exposition**
**IMECE2023**
**October 29–November 2, 2023, New Orleans, LA**

**IMECE2023-112479**

# HYDRO-STRUCTURAL DESIGN EXPLORATION OF FLOATING PLATFORM FOR OFFSHORE ENERGY SYSTEMS

**Chandler S. Cain[1], Yong Hoon Lee[1,*]**

[1]Department of Mechanical Engineering,
The University of Memphis, Memphis, TN

## ABSTRACT

*This paper presents a comprehensive study on the hydro-structural design exploration of floating platforms for offshore energy systems. The study aims to develop a novel design method that optimizes the structure of the platform for stable dynamic responses to ocean waves, ensuring that the motion of the platform remains within acceptable acceleration ranges in all six degrees of freedom, while ensuring satisfactory of geometrical constraints. The study delves into the free-form design of the outer columns of the floating platform beyond conventional predefined shapes to enhance the overall performance of the system. The design utilizes a parameterization based on free-form spline interpolation for the outer shape of the hull and fixed-shaped pontoons to connect to the central structure where the energy-generating device (e.g. wind turbine) is installed. The study employs hydrostatic, hydrodynamic, and time-domain structural dynamic simulations within a monolithic multidisciplinary design optimization formulation to evaluate the overall dynamic responses of floating platforms. Overall, this study provides valuable insights into the hydro-structural design of the floating platforms for offshore energy systems. The optimal shape of the outer column suggests that the concave design enhances dynamic performance by effectively reducing the span-wise footprint of the platform. The results offer design considerations for floating platform hull developers to create robust designs that can withstand harsh metocean conditions. The findings obtained from the optimization solutions suggest the need for advanced design exploration and shape optimization of the floating platform hull, including the pontoons and the central structure for optimal performance. The study also suggests employing manufacturability constraints and wave loadings in all possible directions to reflect real-world operating conditions of floating platforms.*

**Keywords: Hydrodynamics, Rigid Body Dynamics, Floating Platform, Shape Optimization, Design Optimization**

*Corresponding author: yhlee@memphis.edu

## 1. INTRODUCTION

In recent decades, the growing energy demand has highlighted the need for cleaner and more sustainable alternatives to traditional energy generation methods to mitigate the impacts of climate change [1, 2]. Consequently, research into renewable sources of energy production has become essential to minimize the carbon footprint associated with meeting our energy needs [2]. Offshore locations, with their vast and relatively unobstructed expanse, offer an ideal environment for harnessing renewable energy, despite the high capital and operational expenses of floating and mooring devices [3, 4]. To better facilitate economic feasibility, the entire system needs to be highly optimized in terms of both energy generation efficiency and associated expenses [5, 6].

Floating platforms are necessary for the installation of offshore energy systems in deep water regions, where environmental conditions are more consistent and spatial competition is minimal [7]. However, these floating platforms present unique design challenges. First, the cost of a floating platform constitutes a significant portion of the overall expenses in offshore renewable energy systems, exceeding 25 percent of the total capital cost [8]. Second, compact and affordable floating platforms can lead to larger overall system motions (displacement and acceleration) due to reduced hydrostatic stabilities, potentially increasing the total system cost [9].

The system engineering approach with a numerical design optimization method can address these challenges and improve cost efficiency [10]. Previous studies on system design have explored simple design parameters, such as component mass ratio or parametric sizing optimization problems [9, 11, 12]. With the goal of minimizing the levelized cost of energy (LCOE), these studies explored the concurrent design optimization of multiple physics disciplinary domains and component designs along with dynamic control strategies. However, these studies employed relatively simple geometric parameterizations, leaving a significant gap between their optimal solutions and the ideally attainable performances.

Fluid-structure interactions on floating platforms are heavily

influenced by their geometrical shapes, as hydrodynamic forces act in the normal direction of the surface at each point at the fluid-structure interfaces [13]. In many engineering design problems where simple traditional shapes are commonly used, creative parameterization to create non-conventional designs without human-imposed assumptions may enhance system performance by orders of magnitude beyond what was generally available with traditional forms [14, 15]. If we allow greater design freedom beyond typical cylinders and rectangular tube shapes that are prevalently used in floating platform components, the overall hydrodynamic performance of the platform could be significantly enhanced without sacrificing hydrostatic stabilities and cost efficiency. In this study, we aim to initially explore how the free-form design of the floating platform beyond conventional predefined shapes can be posed and explored to enhance the overall system performance. The findings obtained from this study will later be utilized in subsequent studies to redefine floating platform shapes that perform better than conventional designs.

## 2. METHODS

### 2.1 Modeling of the floating body dynamics

The dynamics of the floating platform of interest is represented by a rigid body with six degrees of freedom (6-DOF) dynamic motion framework, subject to various forcing terms. The 6-DOF dynamics of the rigid body platform is governed by a mass-damper-stiffness system of equations, given as:

$$\left(M + M_{a,\infty}\right) \ddot{\xi}_k\left(t\right) + \int_0^t K\left(t-\tau\right) \dot{\xi}_k\left(\tau\right) \mathrm{d}\tau + \left(C+T\right) \xi_k\left(t\right) = F_{\mathrm{FK},k} + F_{\mathrm{D},k} + F_{\mathrm{V},k} \tag{1}$$

for $k \in \{1,2,3,4,5,6\}$, where $M$ is the mass matrix of the system and $M_{a,\infty}$ is the hydrodynamic added mass matrix of the underwater portion of the system. The vector $\ddot{\xi}_k$ represents the floating body acceleration, the vector $\dot{\xi}_k$ represents the floating body velocity, and the vector $\xi_k$ represents the floating body displacement. The index $k$ corresponds to each of the six DOFs, namely the surge, sway, heave, roll, pitch, and yaw directions.

By treating the floating structure (the platform and the energy-generating device) as a single rigid body as a whole, Eq. (1) provides the time-dependent motion trajectories of the entire system. The convolution integral in the second term on the left-hand side represents the hydrodynamic radiation-damping effect. In this convolution integral term, $K$ represents the radiation-retardation kernel, which imparts the force with a memory effect from the structure's velocity-induced waves. On the right-hand side, $F_{\mathrm{FK},k}$ and $F_{\mathrm{D},k}$ are the Froude-Krylov and wave diffraction forces acting on the body in response to incident waves. Finally, $F_{\mathrm{V},k}$ corresponds to the viscous drag force, provided by the drag equation, given as:

$$F_{\mathrm{D},k} = \frac{1}{2}\rho u_k^2 C_{\mathrm{D}} A, \tag{2}$$

where $u_k$ represents the flow velocity, $C_{\mathrm{D}}$ represents the drag coefficient, and $A$ represents the reference area of the submerged portion of the floating body.

The impulsive hydrodynamic added mass tensor represents the virtual inertia added to the system due to the acceleration of the immersed body, and it is a function of frequency. However, for the instantaneous response to acceleration, the infinite frequency hydrodynamic added mass is considered, represented as $M_{a,\infty}$ in Eq. (1). Similarly, the radiation-damping tensor is also frequency-dependent. The wave-retardation kernel $K$ is defined in the time-domain, calculated by integrating the radiation-damping tensor from zero to infinity frequencies for each time point, resulting in an impulse response function.

Here, we utilize the Capytaine code to compute the added impulsive hydrodynamic mass tensor, the radiation-damping coefficient used to calculate the radiation retardation kernel, the Froude-Krylov force, and the diffraction force for each shape of the floating platform design [9, 16]. This code employs linear potential flow wave theory and the boundary element method (BEM) to provide the aforementioned hydrodynamic coefficients in the frequency domain, based on the assumptions of incompressible, inviscid, and irrotational flow. Within the optimization loop, these hydrodynamic forcing terms are computed repeatedly for each individual design point.

The calculation of the hydrostatic forces is performed over a specified range of time, wave frequencies, and direction values to provide a substantial amount of data for the motion analysis. Wave height and period are determined and used to create a statistical wave signal in the time domain using the JONSWAP spectrum [17]. The resulting wave profile contains a wide range of frequencies and amplitudes, making the incident wave loads applied to the floating platform realistic. However, when this method is used for commercial applications the simulation time window needs to be long enough due to the stochastic nature of the waves generated by the JONSWAP spectrum. Since this study focuses mainly on the development of the methodologies as opposed to creating actual solutions for manufacturing, it should be noted that the current formulation does not perform simulations for such an extended time window.

### 2.2 Simulation of the floating body dynamics

Time-domain simulation of the floating platform motion requires solving the state space equation, which is created to form an ordinary differential equation (ODE). The state vector includes both displacement and velocity components of all 6-DOF elements, given as:

$$\boldsymbol{\Xi} = \left[\xi_1, \cdots, \xi_6, \dot{\xi}_1, \cdots, \dot{\xi}_6\right]^{\mathsf{T}}, \tag{3}$$

where $\Xi$ is the state vector representing the second-order ODE represented in a system of first-order ODE form. Solving this ODE involves the construction of system dynamics in the form of derivative function, given as:

$$\dot{\boldsymbol{\Xi}} = \mathbf{f}_d\left(\boldsymbol{\Xi}\right), \tag{4}$$

where $\mathbf{f}_d$ is the derivative function that represents the system dynamics. However, obtaining this function at each time step requires a solution for the convolution integral, given in the second term on the left-hand side of Eq. (1). This requires expensive numerical integration. However, in this wave retardation term, the wave effect would diminish over time and, as a result, it does not affect the dynamic response if we truncate the convolution

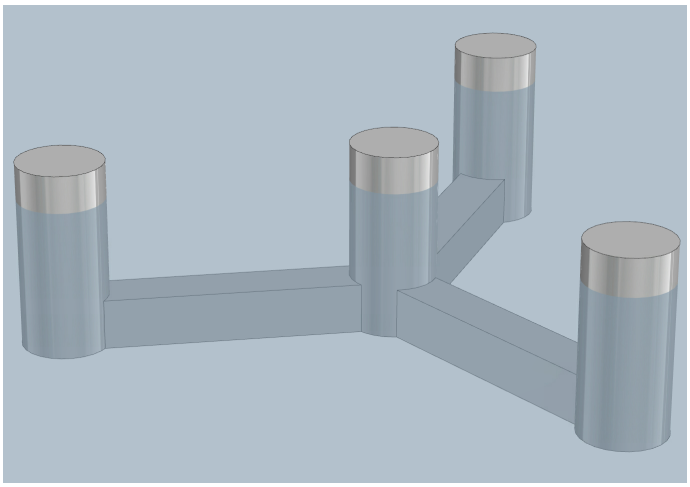

**FIGURE 1: BASELINE FLOATING PLATFORM DESIGN**

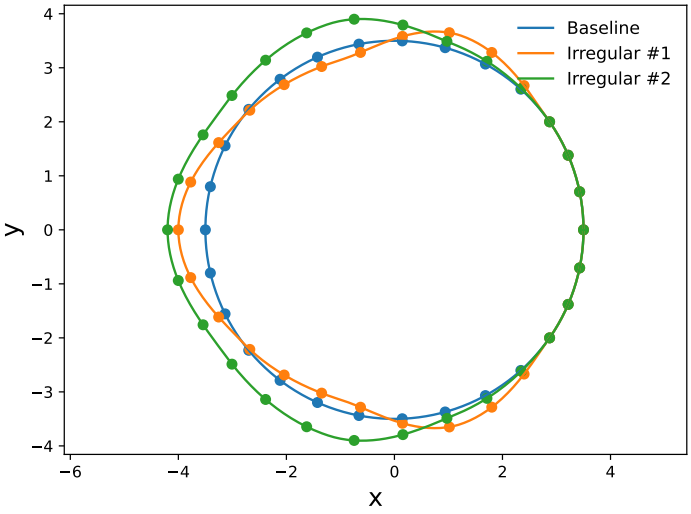


**FIGURE 2: VARIED (CIRCULAR AND IRREGULAR) CROSS-SECTIONAL SHAPES OF THE OUTER COLUMN**

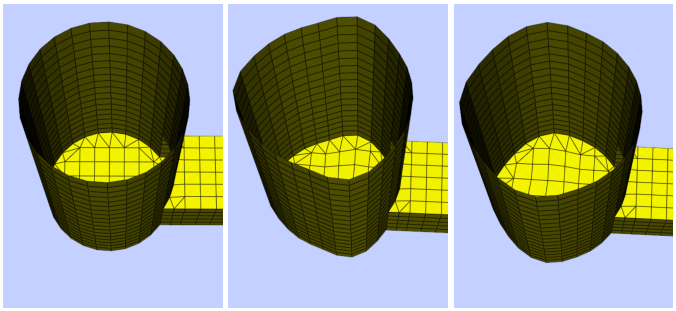


**FIGURE 3: COMPUTATIONAL PANEL BOUNDARY ELEMENT MESHES OF VARIED CROSS-SECTIONAL SHAPES OF THE OUTER COLUMN**

integral for past state trajectories beyond a certain amount of time [18, 19]. Generally, the truncation should be performed after the integration is performed for a sufficient amount of time, and an additional study needs to be conducted to characterize the convolution integral kernel function to systematically identify the amount of truncation time [20].

### 2.3 Floating platform design

A typical semi-submersible or tension leg platform (TLP) design used for floating offshore wind turbines (FOWTs) serves as our baseline floating platform design. The baseline design consists of one center column, three outer columns, and three pontoons that connect the outer columns to the center column. The baseline design is depicted in Fig. 1.

The center column hosts the mounting point for the primary energy-generating device (e.g., wind turbine tower), and the center of gravity of the device is generally located far above the still water line (SWL). We have considered this configuration in constructing our numerical model, placing a virtual mass at a high position above the SWL.

Pontoons are instrumental in maintaining the distances between columns, thereby ensuring stability across three rotational DOFs. However, while increased pontoon length offers enhanced stability, it also becomes more susceptible to the influence of hydrodynamic forces and affects the structural integrity of the system. The columns and pontoons collectively act as a buoy for the structure of the system. Yet, they are simultaneously subject to a variety of hydrodynamic forces, originating from ocean current and incident waves, along with the radiation and diffraction effects of the floating platform.

This study aims to minimize the motion of the floating platform under incident wave loadings by optimizing the shapes of the outer columns. Considering the substantial influence of the submerged structure's shape on the hydrodynamic forces governing fluid-structure interactions and given that the outer columns directly confront wave loadings, we focus on the optimization of their shapes. This serves as our initial step toward a broader objective of comprehensive free-form shape optimization of the entire floating platform, a goal planned to extend beyond the scope of this paper.

### 2.4 Design parameterization

In order to optimize the outer column design, we employ a parameterization method that defines the outline of the cross-sectional shape. This method involves using a spline curve with a select number of control points, and then projecting the outermost mesh nodes on this spline curve, as illustrated in Fig. 2.

Considering that waves can arrive from any direction, asymmetric column designs will likely perform suboptimally. For instance, while an asymmetric design might offer enhanced performance for waves coming from a specific direction, it may fall significantly short in effectiveness for waves coming from other directions. Consequently, we impose a symmetric constraint in our shape formulation, which effectively reduces the number of design variables by half.

Additionally, the mesh nodes shared by both the outer column and the pontoon should not be altered. Therefore, we do not change the outline of the mesh nodes that are connected to the pontoon. This constraint is reflected in Fig. 2, where seven marker

points on the positive side in the $x$ direction are fixed at their original locations.

The vector of design variables includes radii of independent control points from the center of the baseline column, given as:

$$\mathbf{x} = [r_1, r_2, \cdots, r_N]^\mathsf{T}, \tag{5}$$

where $\mathbf{x}$ is the vector of design variables, $r_i$ is the radius of $i$-th control point, and $N$ is the number of independent control points. As explained, due to the symmetric constraint and the outline section shared with the pontoon, we use seven independent control points in this study.

After the outline is defined, the cylindrical column mesh is manipulated to conform to the curvature of the column outline curvature. All inner mesh nodes are stretched (in either extending or contracting directions) in radial directions with respect to the center of the column. This mesh handling technique offers distinct advantages when sensitivity is evaluated by a gradient-based optimizer using finite differencing. By maintaining mesh connectivity and nodal positions in a continuous manner, we can significantly reduce the likelihood of discontinuities in optimization metrics, which include both the objective and constraint functions.

The baseline design given in Fig. 1 has three cylindrical outer columns with a circular cross-sectional shape. The outline profile and the control points of this baseline design (Shape 1) are illustrated as a blue line with markers in Fig. 2, and the corresponding computational mesh is partially shown in Fig. 3a. Two irregular shapes (Shape 2 and Shape 3) are additionally employed to demonstrate the change in the outline of the cross-sectional shapes of the outer columns. The outline profile and the control points of Shape 2 and Shape 3 are illustrated as orange and green lines with markers in Fig. 2, respectively. The corresponding computational meshes are partially shown in Fig. 3b and 3c, respectively.

### 2.5 Optimization formulation

Here, the design optimization problem for the floating platform is formulated as follow:

$$\begin{aligned}
\underset{\mathbf{x}}{\text{minimize:}} \quad & \frac{C_{\text{scaling}}}{t_f - t_0} \sum_{k=1}^{6} \left( \int_{t_0}^{t_f} \ddot{\Xi}_k^2 \, \mathrm{d}t \right)^{\frac{1}{2}} \\
\text{subject to:} \quad & A_{\text{outer-column}}(\mathbf{x}) - A_{\text{outer-column},0} = 0 \\
\text{subject to:} \quad & \sum_{t_0}^{t_f} (\Xi^2)^{1/2} = \sum_{t_0}^{t_f} (\Xi_0^2)^{1/2} \\
\text{where:} \quad & \dot{\Xi} - \mathbf{f}_d(\Xi, \mathbf{x}) = \mathbf{0},
\end{aligned} \tag{6}$$

where $C_{\text{scaling}}$ is a scaling factor that ensures the objective function is not affected by round-off errors, $t_0$ and $t_f$ are the initial and final times of the time-domain simulation, $A_{\text{outer-column}}$ is the cross-sectional area of the outer column and is a function of $\mathbf{x}$, and $A_{\text{outer-column},0}$ is the cross-sectional area of the outer column at the baseline design ($\mathbf{x} = \mathbf{x}_0$).

In this formulation, the objective function aims to minimize the sum of time-averaged platform accelerations across all 6-DOF directions. It is important to note that the acceleration values in each of the six DOFs have unique and significantly different scales. By summing the accelerations over these six DOFs, the optimizer is naturally encouraged to prioritize the design optimization with regard to DOFs characterized by larger scales, while still accounting for contributions from all directions. This approach ensures a balanced and effective optimization process that accounts for the varying impact of each DOF on the overall performance of the floating platform.

An equality constraint is also imposed in this formulation to ensure that the explored design maintains the same cross-sectional area for the columns. This constraint effectively guarantees that the buoyant force of the platform remains constant, preserving the hydrostatic characteristics of the baseline platform design.

Lastly, the time-dependent dynamic simulation is performed externally and independently of the optimizer. The simulation model retrieves the current design under evaluation from the optimizer and supplies the resulting time-dependent trajectories of the state variables, $\xi_k$ and $\dot{\xi}_k$ for all 6-DOFs, where $k \in \{1, 2, 3, 4, 5, 6\}$. The optimizer treats the simulation model as a black-box function and does not handle the dynamic constraint specified in the expression after "where" clause in Eq. (6).

Given that the problem outlined in Eq. (6) takes the form of a nonlinear programming (NLP) problem, we employ the IPOPT nonlinear optimizer [21] for its solution. At this early stage of design exploration, we intentionally set the solver's maximum number of iterations to a small value (maxiter= 10). This approach facilitates the faster acquisition of approximate results, enabling us to discern potential pathways toward enhanced solutions without spending large computational expenses.

**TABLE 1: ANALYSIS AND OPTIMIZATION CASES, INITIAL CONDITIONS, AND SOLUTIONS**

| | Initial condition | Numerical solution | |
|---|---|---|---|
| Case | Shape and radius | Objective function | Constraint violation |
| Analysis 1 | Circular, 3.5 m (Baseline) | 1.374377 | $0.000 \times 10^{0}$ |
| Analysis 2 | Irregular #1 | 1.402011 | $1.564 \times 10^{0}$ |
| Analysis 3 | Irregular #2 | 1.473139 | $6.281 \times 10^{0}$ |
| Optim 1 | Circular, 3.5 m (Baseline) | 1.316513 | $5.332 \times 10^{-3}$ |
| Optim 2 | Circular, 3.4 m | 1.313484 | $2.194 \times 10^{-4}$ |
| Optim 3 | Circular, 3.8 m | 1.320251 | $2.499 \times 10^{-4}$ |
| Optim 4 | Irregular #1 | 1.331540 | $2.549 \times 10^{-4}$ |

## 3. RESULTS AND DISCUSSION

We conducted analyses on three distinctive outline shapes of the outer column designs, including cases with a circular shape with a radius of 3.5 m (Analysis 1) and two arbitrarily-created irregular shapes (Analysis 2 and 3). Furthermore, numerical

**TABLE 2: COMPUTATIONAL EXPENSES**

| Case | Total time elapsed | Number of iterations | Number of fn. evals |
|---|---|---|---|
| Analysis 1 | 3.09 min | N/A | 1 |
| Analysis 2 | 3.02 min | N/A | 1 |
| Analysis 3 | 3.05 min | N/A | 1 |
| Optim 1 | 322.78 min | 10 | 103 |
| Optim 2 | 294.70 min | 10 | 93 |
| Optim 3 | 297.35 min | 10 | 95 |
| Optim 4 | 535.18 min | 10 | 170 |

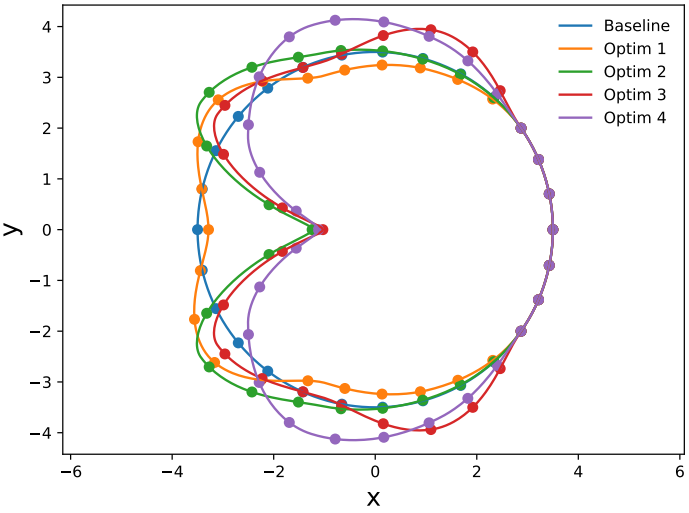


**FIGURE 4: OPTIMAL CROSS-SECTIONAL SHAPES OF THE OUTER COLUMN**

design optimizations were performed with four different initial design points, beginning from circular shapes with three varying radii values (Optim 1–3), and the irregular shape (Irregular #1) utilized in the Analysis 2 case (Optim 4). The case definitions, initial conditions, and numerical solutions are detailed in Tab. 1. The two irregular shapes employed in the Analysis 2, 3, and Optim 4 cases, in comparison to the baseline circular shape, are previously defined in Figs. 2 and 3. Computational expenses in terms of the solution time and the number of function evaluations are given in Tab. 2. The computations were performed using dual Intel Xeon Gold 6242R processors, and parallel computation was extensively utilized in linear potential flow solutions throughout the wide range of wave frequencies.

We note that the optimal solutions for all four cases exhibit convergence towards similar objective function values. The objective function values of the four optimal solutions (Optim 1–4) are 3.11–4.43% lower than the objective function value of the baseline case (Analysis 1). Constraint violations in Tab. 1 are calculated by:

$$\left|A_{\text{outer-column}} - A_{\text{outer-column},0}\right|. \tag{7}$$

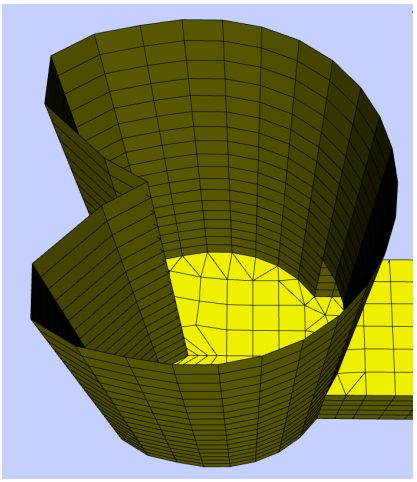

**FIGURE 5: OPTIMAL DESIGN COMPUTATIONAL PANEL BOUNDARY ELEMENT MESH OF THE OUTER COLUMN**

Maximum constraint violation was observed from Optim 1 case, which is $5.332 \times 10^{-3}$. However, this value is only 0.014% of the baseline cross-section area, meaning that the constraint violation is negligible for the solutions of all Optim 1–4 cases.

Figure 4 shows the optimal cross-sectional shapes of the outer column for the Optim 1–4 cases, contrasting them with the baseline design (Analysis 1). Although the objective function values for all four cases are remarkably similar, optimal solutions in terms of the cross-sectional shapes exhibit notably different designs. However, it is evident that the optimal solutions tend to converge toward concave shapes at the outermost location of the platform. Generally, longer pontoons are more susceptible to wave loadings, but they also offer improved hydrodynamic stabilities at the same time. The underlying reasons behind these optimal shapes warrant further investigation. Nontheless, considering the relatively smaller pitching DOF motion in comparison to other two major DOFs due to the characteristics of the TLP, one can hypothesize that the concave and wider outer column shapes may effectively provide benefits similar to those offered by a shorter pontoon design.

Given that the objective function values for all Optim 1–4 cases are similar, we opted to conduct a more thorough investigation on the optimal design solution of the Optim 2 case. This decision was driven by the relatively superior performance of the Optim 2 design in terms of the objective function value, notwithstanding the slight difference compared to the other Optim cases. Figure 5 illustrates the panel BEM mesh pertaining to the optimal design associated with the solution of the Optim 2 case. In this preliminary exploratory study, we did not impose any constraints aside from the constant cross-sectional area stipulated in Eq. (6). However, the optimal shape presented here possesses an extremely sharp transition in the outline surface angle, which could pose manufacturing challenges for the floating platform structure. For future studies, additional constraints, such as the maximum curvature of the surface, should be implemented to circumvent the emergence of such extreme designs as optimal solutions.

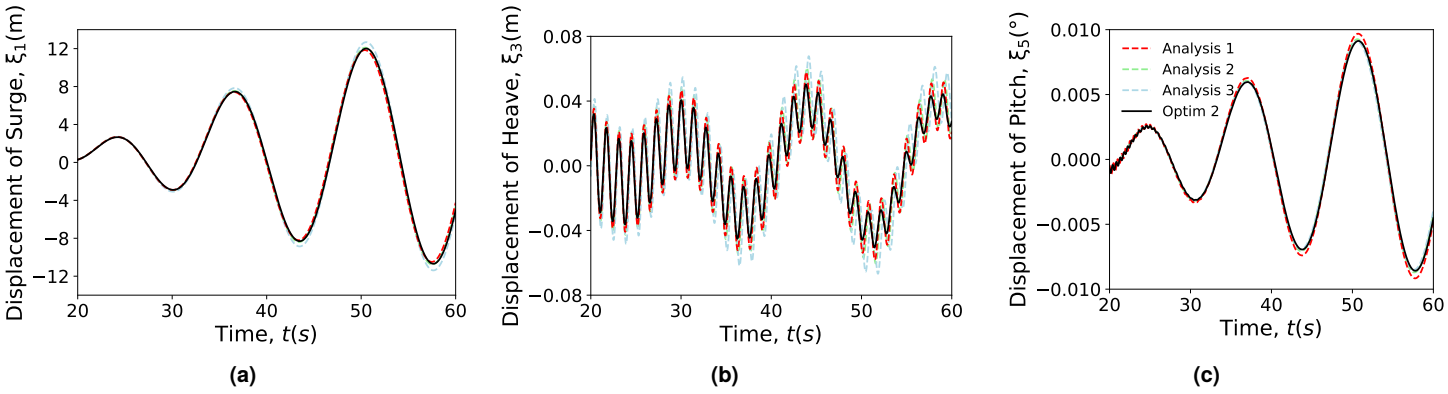


**FIGURE 6: DISPLACEMENT OF FLOATER DESIGNS**

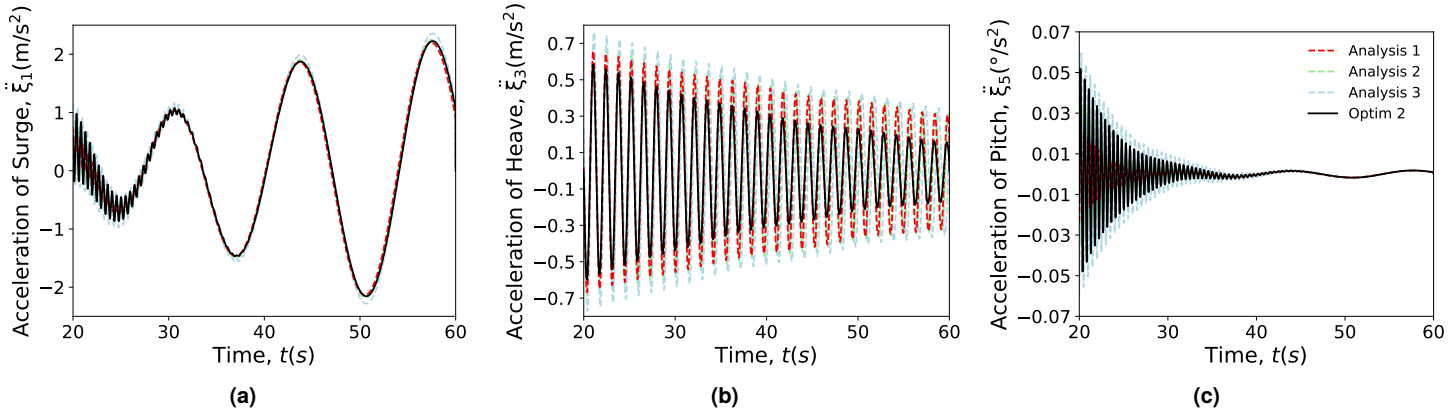


**FIGURE 7: ACCELERATION OF FLOATER DESIGNS**

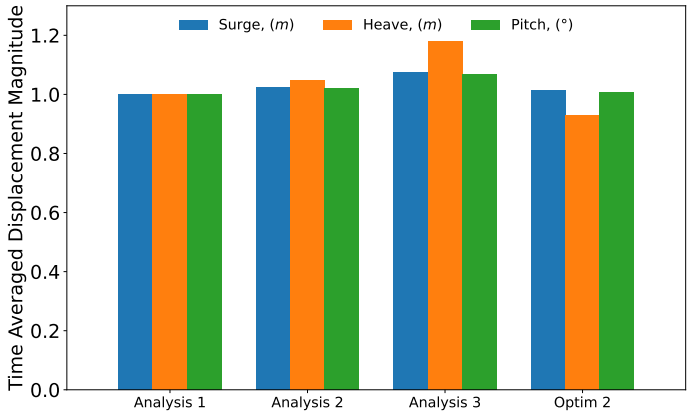


**FIGURE 8: TIME-AVERAGED AND NORMALIZED DISPLACEMENTS FOR FLOATING BODY SURGE, HEAVE, AND PITCH DOFS**

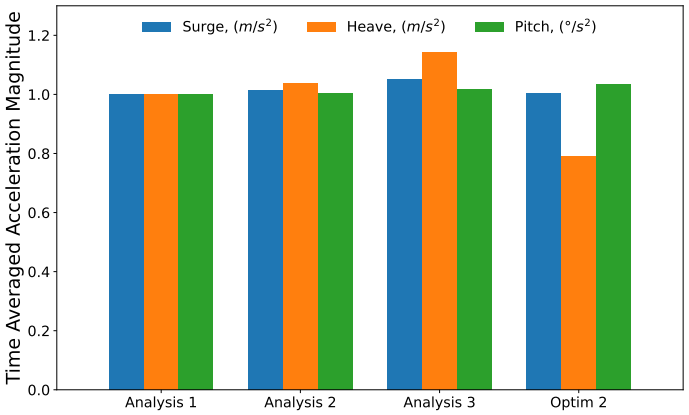


**FIGURE 9: TIME-AVERAGED AND NORMALIZED ACCELERATIONS FOR FLOATING BODY SURGE, HEAVE, AND PITCH DOFS**

Figures 6 and 7 showcase the system displacement and acceleration trajectories in the surge, heave, and pitch DOFs for the Analysis 1, 2, 3 and the Optim 2 cases. When compared to the baseline case (Analysis 1), the arbitrary irregular shapes utilized in the Analysis 2 and 3 cases demonstrate higher amplitudes in both displacement and acceleration trajectories across all DOFs. However, the optimized solution provided by the Optim 2 case exhibits notably reduced amplitudes in both displacement and acceleration trajectories for the heave DOF motion, albeit at the expense of slight increase in the amplitudes of the pitch DOF motion. This finding supports our previously proposed hypothesis, suggesting that the concave and wider outer column shapes might offer enhanced performance under wave loadings with a small sacrifice in the stability due to a reduced effective span footprint (similar to shorter pontoon length).

Figures 8 and 9 depict the time-averaged displacement and

acceleration magnitudes within the surge, heave, and pitch DOFs for the instances of Analysis 1, 2, 3 and the Optim 2 cases. The bar graphs are normalized to the results of the baseline case. Thus, the baseline case magnitudes are 1.0 for all DOFs. These figures clearly displays the average magnitude relative to the baseline case. Arbitrarily-created irregular shapes (Analysis 2 and 3) exhibit inferior performances in all DOFs in terms of both displacement and acceleration. However, Optim 2 result exhibit a significantly reduced displacement and acceleration in the heave DOF, with a slightly increased acceleration in the pitch DOF, as we dicussed above.

The computational results presented here are evaluated solely based on the incoming wave from negative to positive $x$ direction, a strategy to maintain computational efficiency. Readers are directed to Figs. 2 and 4 for a clear understanding of the direction of the $x$ axis. However, for a more comprehensive representation of real-world conditions, it is imperative to consider incoming waves from all possible directions within the optimization loop. While this would undoubtedly escalate the computational overhead in terms of CPU hours, the employment of a parallel processing framework would prevent any substantial increase in total computational time. Consequently, future research must take into account the arbitrary character of the incoming wave direction.

## 4. CONCLUSION

When formulating the floating platform design problem, the key hypothesis was considered that the outer column of the floating platform would exert the most significant influence on the hydrodynamic interactions between the floating platform motion and its surrounding environment. This supposition stemmed from the fact that the outer columns, which provide the main buoyant force and stability of the system, would be subjected to the primary forces imparted by the incoming waves. Consequently, the optimization focus was directed towards the outer shape, as it was believed that modifying this aspect would yield the most substantial impact beyond the original design.

The optimal solutions obtained from Optim 1–4 cases support this key hypothesis. The solution proposes that the outer column adopt a concave shape at the outermost location to minimize acceleration in the heave direction, while tolerating a minor increase in acceleration in the pitch direction. By this means, the overall acceleration of the floating platform's motion could be substantially curtailed.

The findings advocate for an expanded scope of design exploration beyond the shape optimization of the outer column. The logical next step would involve incorporating all submerged structures into the design optimization process and permitting comprehensive free-form shape optimization utilizing advanced design parameterization techniques.

## REFERENCES


[1] Wiser, Ryan H. "Green power marketing: Increasing customer demand for renewable energy." *Utilities Policy* Vol. 7 No. 2 (1998): pp. 107–119. DOI 10.1016/S0957-1787(98)00005-8.

[2] Hasanuzzaman, M., Zubir, Ummu Salamah, Ilham, Nur Iqtiyani and Seng Che, Hang. "Global electricity demand, generation, grid system, and renewable energy polices: A review." *WIREs Energy and Environment* Vol. 6 No. 3 (2017): p. e222. DOI 10.1002/wene.222.

[3] Weiss, Carlos V. C., Guanche, Raúl, Ondiviela, Bárbara, Castellanos, Omar F. and Juanes, José. "Marine renewable energy potential: A global perspective for offshore wind and wave exploitation." *Energy Conversion and Management* Vol. 177 (2018): pp. 43–54. DOI 10.1016/j.enconman.2018.09.059.

[4] Schwartz, Marc, Heimiller, Donna, Haymes, Steve and Musial, Walt. "Assessment of Offshore Wind Energy Resources for the United States." Technical Report No. NREL/TP-500-45889. National Renewable Energy Laboratory, Golden, CO. 2010. DOI 10.2172/983415.

[5] Johnston, Barry, Foley, Aoife, Doran, John and Littler, Timothy. "Levelised cost of energy, A challenge for offshore wind." *Renewable Energy* Vol. 160 (2020): pp. 876–885. DOI 10.1016/j.renene.2020.06.030.

[6] Garcia-Sanz, Mario. "A metric space with LCOE isolines for research guidance in wind and hydrokinetic energy systems." *Wind Energy* Vol. 23 No. 2 (2020): p. 291–311. DOI 10.1002/we.2429.

[7] Hélène, Buchholzer, Marjolaine, Frésard, Christelle, Le Grand and Le Floc'h, Pascal. "Vulnerability and spatial competition: The case of fisheries and offshore wind projects." *Ecological Economics* Vol. 197 (2022): p. 107454. DOI 10.1016/j.ecolecon.2022.107454.

[8] Butterfield, S., Musial, W., Jonkman, J. and Sclavounos, P. "Engineering challenges for floating offshore wind turbines." *Copenhagen Offshore Wind Conference*: pp. 1–10. 2005. Copenhagen, Denmark.

[9] Lee, Yong Hoon, Boo, Sung Youn and Allison, James T. "A framework for integrating hydrostatics, hydrodynamics, and rigid-body dynamics for the control co-design of floating offshore vertical-axis wind turbine systems." *Wind Energy Science Conference*. 2021. Hannover, Germany.

[10] Barter, Garrett E., Robertson, Amy and Musial, Walter. "A systems engineering vision for floating offshore wind cost optimization." *Renewable Energy Focus* Vol. 34 (2020): pp. 1–16. DOI 10.1016/j.ref.2020.03.002.

[11] Abdelmoteleb, Serag-Eldin, Mendoza, Alejandra S. Escalera, dos Santos, Carlos R., Bachynski-Polić, Erin E., Griffith, D. Todd and Oggiano, Luca. "Preliminary sizing and optimization of semisubmersible substructures for future generation offshore wind turbines." *Journal of Physics: Conference Series* Vol. 2362 (2022): p. 012001. DOI 10.1088/1742-6596/2362/1/012001.

[12] Sundarrajan, Athul K., Lee, Yong Hoon, Allison, James T. and Herber, Daniel R. "Open-loop control co-design of floating offshore wind turbines using linear parameter-varying models." *ASME IDETC/CIE, Design Automation Conference*. DETC2021-67573. 2021. ASME, Virtual, Online. DOI 10.1115/DETC2021-67573.

[13] Newman, J. N. *Marine Hydrodynamics*, 40th Anniversary ed. MIT Press, Cambridge, MA (2018).

[14] Lee, Yong Hoon, Schuh, Jonathon K., Ewoldt, Randy H. and Allison, James T. "Enhancing full-film lubrication per-

formance via arbitrary surface texture design." *Journal of Mechanical Design* Vol. 139 No. 5 (2017): p. 053401. DOI 10.1115/1.4036133.

[15] He, Xiaolong, Li, Jichao, Mader, Charles A., Yildirim, Anil and Martins, Joaquim R. R. A. "Robust aerodynamic shape optimization—From a circle to an airfoil." *Aerospace Science and Technology* Vol. 87 (2019): pp. 48–61. DOI 10.1016/j.ast.2019.01.051.

[16] Ancellin, Matthieu and Dias, Frédéric. "Capytaine: a Python-based linear potential flow solver." *Journal of Open Source Software* Vol. 4 No. 36 (2019): p. 1341. DOI 10.21105/joss.01341.

[17] Hasselmann, K., Barnett, T. P., Bouws, E. et al. "Measurements of wind-wave growth and swell decay during the Joint North Sea Wave Project (JONSWAP)." Technical report no. Deutches Hydrographisches Institut, Hamburg, Germany. 1973.

[18] Jonkman, Jason M. "Dynamics of offshore floating wind turbines—model development and verification." *Wind Energy* Vol. 12 No. 5 (2009): pp. 459–492. DOI https://doi.org/10.1002/we.347.

[19] Lee, Yong Hoon, Vedant, Ewoldt, Randy H. and Allison, James T. "Strain-actuated solar arrays for spacecraft attitude control assisted by viscoelastic damping." *Advances in Structural and Multidisciplinary Optimization, Proceedings of the 13th World Congress of Structural and Multidisciplinary Optimization*: pp. 149–155. 2019. Dalian University of Technology Electronic & Audio-Visual Press, Dalian, China.

[20] Adolfsson, Klas, Enelund, Mikael and Larsson, Stig. "Adaptive discretization of an integro-differential equation with a weakly singular convolution kernel." *Computer Methods in Applied Mechanics and Engineering* Vol. 192 No. 51–52 (2003): pp. 5285–5304. DOI 10.1016/j.cma.2003.09.001.

[21] Wächter, Andreas. "An interior point algorithm for large-scale nonlinear optimization with applications in process engineering." Ph.D. Thesis, Carnegie Mellon University, Pittsburgh, PA. 2002.